Plausibility of lunar crustal magmatism producing strong crustal magnetism

Y. Liang[1], S. M. Tikoo[2], M. J. Krawczynski[1]

[1]Department of Earth and Planetary Sciences, Washington University in St. Louis, 1 Brookings Drive, St. Louis, MO 63130.

[2]Department of Geophysics, Stanford University, 397 Panama Mall, Stanford, CA 94305.

Corresponding author: Yuanyuan Liang, (yuanyuanliang@wustl.edu)

Key Points:

- Ilmenite reduction experiments were run at a wide range of experimental conditions
- Subsolidus reduction of ilmenite at lunar conditions creates magnetizable products
- Swirl magnetic source bodies may be caused by the cooling of high-Ti basaltic dikes

Abstract

The Moon generated a long-lived core dynamo magnetic field, with intensities at least episodically reaching ~10–100 μT during the period prior to ~3.56 Ga. While magnetic anomalies observed within impact basins are likely attributable to the presence of impactor-added metal, other anomalies such as those associated with lunar swirls are not as conclusively linked to exogenic materials. This has led to the hypothesis that some anomalies may be related to magmatic features such as dikes, sills, and laccoliths. However, basalts returned from the Apollo missions are magnetized too weakly to produce the required magnetization intensities (>0.5 A/m). Here we test the hypothesis that subsolidus reduction of ilmenite within or adjacent to slowly cooled mafic intrusive bodies could locally enhance metallic FeNi contents within the lunar crust. We find that reduction within hypabyssal dikes with high-Ti or low-Ti mare basalt compositions can produce sufficient FeNi grains to carry the minimum >0.5 A/m magnetization intensity inferred for swirls, especially if ambient fields are >10 μT or if fine-grained Fe-Ni metals in the pseudo-single domain grain size range are formed. Therefore, it is plausible that the magnetic sources responsible for long sublinear swirls like Reiner Gamma and Airy may be magmatic in origin. Our study highlights that the domain state of the magnetic carriers is an under-appreciated factor in controlling a rock's magnetization intensity. The results of this study will help guide interpretations of lunar crustal field data acquired by future rovers that will traverse lunar magnetic anomalies.

Plain Language Summary

While the Moon does not have a magnetic field today, some parts of its crust such as impact basins and bright and sinuous features called "lunar swirls" are still magnetized. Strongly magnetized regions observed within impact basins could be related to iron-rich material derived

from impactors. However, other magnetized regions, such as those associated with lunar swirls, are not as conclusively linked to externally added materials. It has been proposed that the strongly magnetic regions associated with lunar swirls are related to lunar igneous intrusive rocks. Here we experimentally test the hypothesis that the thermal alteration of FeTiO3 grains to TiO2 grains and metallic iron within or next to slowly cooled igneous intrusive features while the Moon had a magnetic field, could explain the strong magnetic regions associated with lunar swirl. We show that the lunar swirl minimum magnetization intensity can be reached from the thermal alteration of ilmenite, especially if ambient fields are strong enough or if fine-grained Fe-Ni metals are formed. This study will help interpret data acquired by future rovers traversing magnetic anomalies on the lunar surface.

1 Introduction

Paleomagnetic studies have suggested that the Moon may have generated a core dynamo magnetic field at least intermittently between ~4.25 Ga and ~1.5 Ga, with intensities reaching ~40–110 μT prior to ~3.56 Ga (Weiss and Tikoo, 2014; Tikoo and Evans, 2022; Wieczorek et al., 2022). The absence of magnetization within young lunar breccias suggests that the dynamo likely ceased between 1.92 and 0.80 Ga ago (Mighani et al., 2020). Whether the dynamo operated continuously and exactly when the lunar dynamo ceased remain uncertain (Evans et al., 2018; Tarduno et al., 2021) . The dynamo history of the Moon is also evident from its remanent crustal magnetism (Hood, 2011; Hood et al., 2021; Purucker et al., 2012; Wieczorek et al., 2022). Intense magnetic anomalies within impact basins are likely caused by impactor-added metal within melt sheets (Oliveira et al., 2017), but anomalies associated with lunar swirls such as the archetypal Reiner Gamma (Denevi et al., 2016; D. Hemingway & Garrick-Bethell, 2012) and

Airy albedo features (David T. Blewett et al., 2011) are more difficult to unequivocally attribute to exogenic metal.

The bulk of remanent magnetization on the Moon is likely recorded within grains of metallic iron and iron-nickel alloys within crustal and upper mantle rocks (Weiss & Tikoo, 2014; Wieczorek, 2018). Anomalies on the southern lunar farside have variably been hypothesized to be related to metal-rich ejecta from the South Pole-Aitken impactor (Wieczorek et al., 2012) or strongly magnetized mafic dikes (Purucker et al., 2012). However, the origin of magnetization at lunar swirls is even more enigmatic because swirls frequently lack correlations with distinct geological features (Denevi et al., 2016). It is hypothesized that swirl-affiliated magnetic anomalies could be related to buried impact melt sheets, impactor-derived ejecta, and iron-rich dikes (Garrick-Bethell & Kelley, 2019; D. J. Hemingway & Tikoo, 2018). However, basalts returned from Apollo missions are generally weakly magnetized (<0.01 A/m) (Wieczorek et al., 2012) and are incapable of producing the magnetization intensities required for swirl formation (>0.5 A/m) (D. J. Hemingway & Tikoo, 2018). It was recently proposed that subsolidus reduction of ilmenite and other minerals within or adjacent to mafic dikes that cooled very slowly (over thousands of years depending on dike width) could produce elevated iron metal contents within the lunar crust (D. J. Hemingway & Tikoo, 2018). Following the approach of Oliveira et al. (2017), Hemingway and Tikoo (2018) determined that reaching magnetization intensities of >0.5 A/m (assuming a 1-km magnetic source thickness) requires rocks to contain >0.3 wt. % Fe-metal. Mare basalts typically have lower metal contents of ~0.08 wt. % Fe (Gose & Butler, 1975). However, Hemingway and Tikoo (2018) calculated that in the extreme case where all ilmenite in a mare basalt were to be converted to Fe + TiO_2, rocks of basaltic composition could be enriched by up to 11 wt.% Fe. Due to uncertainties regarding the rates of

thermochemical alteration of ilmenite, it is unclear whether subsolidus reduction could produce iron concentrations high enough to be consistent with anomalies present at swirls. In this study, we experimentally test the hypothesis that subsolidus reduction of ilmenite can enhance metallic FeNi contents within the lunar crust when it occurs in or near cooled mafic intrusive bodies.

2 Experimental and Analytical procedures

2.1 Starting Material

We used a kimberlitic ilmenite megacryst from Kumgbo, Liberia as the starting material. These natural samples were described in Haggerty (2017), and there were two classes of ilmenite: high-Mg and low-Mg class. The sample we were using for starting material was a high-Mg end member. The high-Mg ilmenite had the lowest amount of ferric iron and was a better match for lunar ilmenites which are Mg-rich (up to 6 wt.%) and ferric-iron-poor (Mason & Melson, 1970). The ilmenite megacryst was homogeneous before the reduction experiments (Fig. 1a).

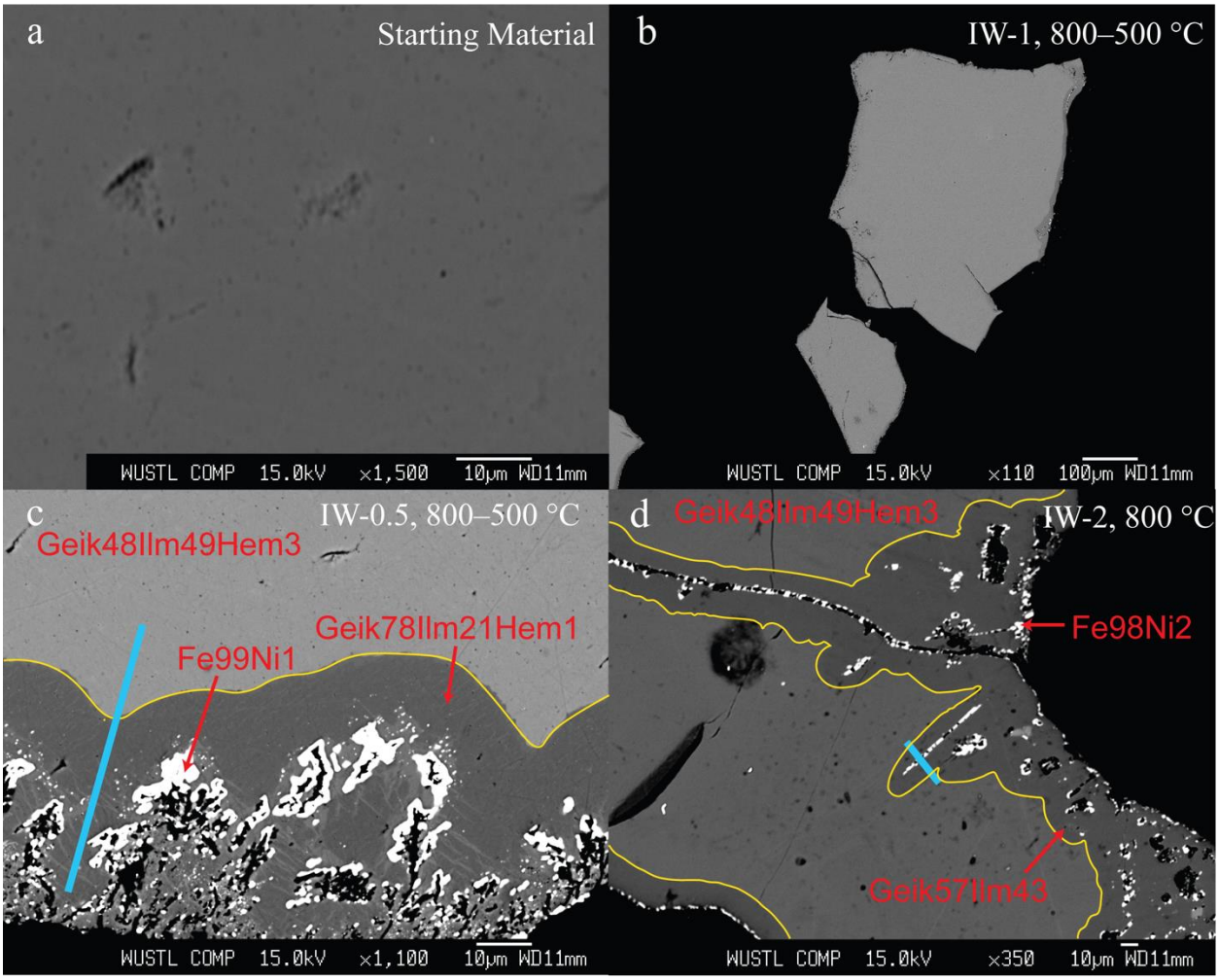

Fig. 1: a. a representative backscatter electron image of a 1500 X view on ilmenite starting material. b. Backscatter electron image of a 110 X view of experimental run H182_S (fO_2 = IW-1 cooling experiment from 800–500 ºC by 3 ºC/hour) showing both homogeneous non-reacted middle area and reacted rim. c. Backscatter electron image of experimental run H171 (fO_2 = IW-0.5 cooling experiment from 800–500 ºC by 3 ºC/hour). The dendritic high reflectance material is FeNi metal formed via subsolidus reduction of ilmenite, and the metal blebs were formed along with the rutile within the reaction zone. Yellow lines separated the light grey unreacted starting material zone from the dark grey reaction zone. A linear traverse of electron microprobe analyses crossing non-reacted to reacted zones was taken to study the compositional difference (blue line). d. Backscatter electron image of experimental run H158 (fO_2 = IW-2 isothermal experiment run at 800 ºC). The colors were the same as in c.

2.2 Experimental Setup

Ilmenite reduction experiments were performed in one-atmosphere gas-mixing vertical tube furnaces at a wide range of durations, quenching temperatures, and grain size of starting

material. Samples were suspended in Re baskets. The Re-wire basket is then attached to a small-diameter Pt quench wire hanging from two thicker Pt electrodes as part of a sample holder assembly. Before the sample holder was inserted into the furnace, the temperature and fO_2 of the system were set at the desired experimental conditions. The temperature during an experiment was monitored by two R-type thermocouples that were calibrated against the melting point of gold and had an estimated accuracy of ± 2°C. Oxygen fugacity was controlled using an H_2-CO_2 gas mixture in all experiments. The fO_2 of each experiment was monitored in situ using a yttria-doped oxygen sensor from Ceramic Oxide Fabricators, with an estimated accuracy of ±0.05 logfO_2 units. Three batches of experiments were performed: 1) time series of isothermal reduction experiments at constant fO_2, 2) cooling series at constant fO_2, and 3) a series with constant fO_2 and cooling histories but differing ilmenite grain sizes (Table 1). For the first batch of experiments, all experiments were conducted at 800 °C and fO_2 = IW-1 with different time duration (2 days, 4 days, 8 days, and 16 days). Ilmenite grain sizes for the first batch of experiments ranged between 1–3 mm. For the second batch of cooling experiments, we used multiple cooling paths. One experiment involved heating ilmenite at 800 °C for 48 hours and then cooling it to 500 °C at a rate of 3 °C/hour (fO_2 = IW-0.5) (experimental run H171), while a second experiment in this batch involved heating at 1000 °C for 48 hours and then cooling to 500 °C at a rate of 3 °C/hour (fO_2 = IW-1) (experimental run H174). The fO_2 sensor was removed before the temperature dropped below 800 °C for the cooling experiments to protect the fO_2 sensor. The fO_2 sensor was only rated for below 1200 mV and decreasing temperature would increase the absolute mV values to greater than 1200 mV. In the third batch of experiments ilmenite grain sizes were systematically varied. In addition to 1–3 mm ilmenite chips, we also

included 10–15 0.5 mm diameter ilmenite pieces in these two experiments. For the third batch of experiments with different grain sizes of ilmenite (experimental runs H181 and H182), all experiments were heated at 800 ^{o}C for 48 hours and then cooled to 500 ^{o}C at 3 ^{o}C/hour (fO_2 = IW-1). The fO_2 sensor was removed before the temperature dropped below 800 ^{o}C during these experiments as well. Since the degree of subsolidus reduction may depend on the exposed surface area to volume ratio of a given ilmenite grain, the starting materials for each set of experiments were divided into small, medium, and large to study the relationship between starting materials' grain sizes and magnetization properties. Experimental runs H181_S and H182_S involved ilmenite grain sizes ranging between 0.5–1.0 mm in diameter. Ilmenite grain sizes in runs H181_M and H181_M were between 1.2–1.6 mm in diameter. Finally, starting materials grain sizes in runs H181_L and H181_L ranged between ~2.0–4.0 mm in diameter. Table 1 summarized the run conditions including the initial temperature, duration, cooling rate, grain size, oxygen fugacity, and experimental temperatures for all experiments.

Table 1: Run conditions and hysteresis analyses of starting materials and experimental run products

Exp	Temp (°C)	fO_2	Duration (days)	Ilmenite Diameter (mm)	M_s (Am^2/kg)	M_{rs} (Am^2/kg)	M_{rs}/M_s	B_c (mT)	B_{cr} (mT)	B_{cr}/B_c	Geik	Ilm	Hem	Hysteresis Mass (mg)
S.M.				~1–3	n /a	0.00	n /a	0.00	n /a	n /a	48.65	48.77	2.58	34
H155	800	IW-1	16	~1–3	3.43×10^{-2}	1.65×10^{-3}	4.81×10^{-2}	16.90	174.00	10.30	52.41	45.79	1.80	14
H154	800	IW-1	4	~1–3	3.20×10^{-2}	2.50×10^{-3}	7.80×10^{-2}	17.70	75.00	4.24				21
H158	800	IW-2	4	~1–3	1.94	5.24×10^{-2}	2.70×10^{-2}	2.30	22.00	9.57	57.17	43.10	0.00	28
J137	800	IW-1	8	~1–3	7.31×10^{-3}	8.23×10^{-4}	1.13×10^{-1}	18.40	62.00	3.37	50.95	49.44	0.00	32
J138	800	IW-1	2	~1–3	5.50×10^{-3}	1.17×10^{-3}	2.13×10^{-1}	27.10	300.00	11.07	50.33	46.32	3.35	17
H171	800–500	IW-0.5	6.2	~1–3 (3), ~0.5 (10)	8.13	6.50×10^{-1}	8.01×10^{-2}	4.10	10.00	2.44	78.43	21.00	0.57	9
H174	1000–500	IW-1	8.9	~1–3 (3), ~0.5 (15)	4.13×10^{-1}	1.20×10^{-2}	2.90×10^{-2}	4.80	47.00	9.79	51.15	48.43	0.41	10
H181_S	800–500	IW-1	6.2	0.86–0.47	4.78×10^{-1}	8.55×10^{-2}	1.79×10^{-1}	13.70	46.30	3.38	64.35	33.08	2.57	31
H181_M	800–500	IW-1	6.2	1.37–1.11	2.77×10^{-1}	4.91×10^{-2}	1.77×10^{-1}	16.30	53.20	3.26				31
H181_L	800–500	IW-1	6.2	3.97–1.96	2.40×10^{-1}	4.50×10^{-2}	1.88×10^{-1}	8.70	33.60	3.86				31
H182_S	800–500	IW-1	6.2	1.09–0.52	1.41	1.33×10^{-1}	9.43×10^{-2}	6.00	14.80	2.47	62.11	34.22	3.66	19
H182_M	800–500	IW-1	6.2	1.61–1.23	8.41×10^{-1}	8.15×10^{-2}	9.69×10^{-2}	5.30	27.00	5.09	62.21	34.78	3.01	31
H182_L	800–500	IW-1	6.2	3.97–1.96	6.66×10^{-1}	6.08×10^{-2}	9.13×10^{-2}	4.80	16.60	3.46				31

Note: S.M. stands for starting material. Experimental runs H171 and H174 were held at 800 °C and 1000 °C respectively for 48 hours then cooled to 500 °C by 3 °C/hour; experimental runs H181 and H182 were held at 800 °C for 48 hours and then cooled by 3 °C/hour to 500 °C. Geikielite, ilmenite, and hematite compositions were approximated because they were calculated from EPMA spot analyses. See Supplementary Materials on how Geik, Ilm, and Hem compositions were calculated.

Rock magnetic experiments (magnetic hysteresis and backfield remanence) were performed on ilmenite starting material as well as reduced products using a LakeShore 8600 Vibrating Sample Magnetometer (VSM) instrument at the Institute for Rock Magnetism at the University of Minnesota. These experiments elucidate the grain size of magnetic minerals and the magnetization carrying capacity of a sample. During a magnetic hysteresis experiment, a sample was placed within a VSM in an initially zero field. The field (B) was increased to an intensity of +1 Tesla (T) in the positive direction, before being reduced in intensity and then applied in the reverse direction to the same intensity (i.e., -1 T) prior to cycling the field back up to +1 T. During the hysteresis experiment, the magnetization intensity of the sample (M) was continuously measured. Magnetic hysteresis properties were obtained following a slope correction to remove paramagnetic contributions. M_s is the saturation magnetization (the strongest magnetization the ferromagnetic component of a sample can contain, in the presence of a saturating field). M_{rs} is the saturation remanent magnetization (the residual remanence after a saturating field is removed). B_c is the coercive field (a measure of the ability to withstand an external field without becoming remagnetized). During backfield experiments, a sample is imparted with a saturating +1 T magnetization in one direction. Then direct fields are applied in the opposite orientation with increasing magnitude to -1 T. B_{cr} is the coercivity of remanence (a measure of the required magnetic field to null an initial saturation remanent magnetization acquired from a field with opposite orientation) (Day et al., 1977). Here we used M_{rs} to help quantify the remanence-carrying ability of ferromagnetic material produced during our subsolidus reduction experiments. Hysteresis and backfield data were processed using the HystLab software package (version 1.0.10) written for MATLAB (Paterson et al., 2018). Values of M_s, M_{rs}, B_c, and B_{cr} for each experiment were shown in Table 1.

175 2.3 Post-experimental material characterization

176 After the reduction experiments, samples were studied by an electron microprobe and a
177 petrographic microscope. Concentrations of major elements in experimental products were
178 analyzed using a JEOL JXA-8200 electron microprobe equipped with five wavelength-dispersive
179 spectrometers, and a JEOL (e2v / Gresham) silicon-drift energy-dispersive spectrometer at
180 Washington University in St. Louis. Analyses were acquired using Probe for EPMA software.
181 A focused beam (~1 μm in diameter) with a current of 25 nA at a 15 kV accelerating voltage was
182 used to measure the concentrations of oxides and Fe-Ni metals. Background X-ray corrections
183 were performed on glass using the mean atomic number correction (Carpenter, 2016).

184

185 **3 Results**

186 3.1 Ilmenite subsolidus reaction products

187 The ilmenite megacryst appeared homogeneous before reduction (a characteristic BSE
188 image of the sample is shown in Fig. 1a). The composition of the starting material was on
189 average 54.98 wt.% Geikielite, 40.56 wt.% ilmenite, and 4.46 wt.% hematite. EPMA analyses of
190 starting materials and experimental run products were reported in Table 2. After reduction
191 experiments, there were reaction zones along the edges of the sample chips and along pre-
192 existing cracks. The reduced megacryst material was darker than the non-reacted starting
193 material area in BSE images indicating it is more Mg-rich, and the reaction rims are ~10–50 μm
194 wide (Fig. 1b–d). Reaction products consisted of pure ilmenite (i.e., no hematite solid solution),
195 Cr-spinel, rutile exsolution, and 1–10 μm diameter nodules of kamacite (α-$Fe_{1-x}Ni_x$ for $x < \sim 0.05$)
196 (Fig. 1c and 1d, Table 3). For the experiment run at fO_2 = IW-0.5 and had a cooling history of
197 800–500 ^{o}C (experimental run H171), the composition of the reaction zone changed from

198 Geik48Ilm49Hem3 of the starting material to Geik78Ilm21Hem1. There were 1–10 μm metals
199 present in the reaction zone, and the average composition of metal was Fe99Ni1 (kamacite).
200 Rutile veins were visible within reaction zones (Fig. 1c). The presence of rutile was confirmed
201 by EPMA and had a composition of pure TiO_2 (Fig. 2a). The composition of the reaction zone
202 changed from Geik48Ilm49Hem3 of the starting material to Geik57Ilm43 for an experiment run
203 at fO_2 = IW-2 and 800 ^{o}C (Experimental run H158). BSE images reveal abundant 1–3 μm metal
204 grains found in the reaction zones (Fig. 1d). The average composition of the metal was Fe98Ni2
205 (kamacite).

Table 2: EPMA analyses of starting materials and experimental run products in oxide weight percent

	No. of analyses	SiO_2		TiO_2		Al_2O_3		Cr_2O_3		FeO		MnO		MgO		CaO		NiO		ZnO		Na_2O		K_2O		Total
S.M.	41	0.00	0.08	55.02	0.26	0.65	0.07	1.92	0.03	27.55	0.27	0.26	0.02	14.37	0.08	0.03	0.04	0.21	0.02	0.02	0.02					100.01
H155	4	0.07	0.18	56.12	1.05	0.58	0.21	2.03	0.60	25.83	1.08	0.26	0.02	14.44	0.23	0.04	0.01	0.75	1.17	0.04	0.02					100.16
H158	10	0.00	0.07	58.37	1.63	0.81	0.54	2.07	1.27	22.09	0.41	0.36	0.05	16.97	0.13	0.07	0.03	0.04	0.04	0.01	0.03					100.79
J137	3	0.00	0.01	57.42	1.89	0.48	0.42	1.83	1.29	25.42	0.17	0.27	0.02	14.98	0.23	0.03	0.01	0.12	0.01	0.01	0.02					100.50
J138	4	0.03	0.05	55.45	0.14	0.80	0.17	1.94	0.02	27.96	0.33	0.26	0.01	15.02	0.26	0.03	0.02	0.22	0.02	0.04	0.01					101.76
H171	6	0.00	0.02	61.37	0.70	0.50	0.17	1.95	0.38	11.96	0.76	0.48	0.03	23.84	0.67	0.02	0.01	0.03	0.01	0.03	0.03	0.02	0.01	0.00	0.00	100.17
H174	4	0.00	0.02	58.43	0.26	0.19	0.09	0.73	0.16	25.57	0.21	0.29	0.04	14.85	0.15	0.03	0.01	0.06	0.07	0.02	0.03	0.05	0.03	0.01	0.01	100.18
H181_S	3	0.00	0.08	58.82	0.20	0.51	0.11	1.63	0.58	20.10	0.49	0.31	0.03	19.01	1.00	0.02	0.01	0.00	0.01	-0.01	0.02	0.03	0.03	0.00	0.01	100.40
H182_S	9	0.00	0.03	57.71	0.75	0.87	0.51	2.19	0.70	20.57	0.90	0.31	0.03	18.18	0.56	0.01	0.01	0.02	0.01	0.03	0.03	0.01	0.02	0.00	0.00	99.87
H182_M	2	0.10	0.05	56.49	0.69	1.04	0.35	3.18	1.29	20.99	0.09	0.29	0.00	18.84	0.79	0.01	0.00	0.04	0.02	0.05	0.00	0.05	0.01	0.00	0.00	101.08

Note: All 41 EPMA points of the starting materials were reported in this table because of their homogeneity. For the reduction experiments, we reported the average compositions and their one standard deviation of the top 10% highest geikielite components of the total analyses of each experimental run. The analyses in this table were taken from the reaction zone on the grains. Columns on the right of each oxide were each oxide's one standard deviation from the number of analyses for each experimental run. The full EPM spot analyses of the starting materials and each experimental run can be found in the Supplementary Materials. Experimental runs H154, H181_M, H181_L, and H182_L were not analyzed by the EPMA, but their hysteresis analyses were reported in Table 1.

Table 3: Metal compositions (at.%) for experiments that formed > 5 μm metals

	No. of analyses	Fe*	Ni*
H158	12	97.99	2.01
H171	5	99.28	0.72
H182_M	7	98.38	1.62
H182_L	1	98.59	1.41

Note: *These compositions were approximated because they were calculated from EPMA spot analyses that overlapped with ilmenite. The FeNi metals were all close to the bcc regime and not close to the fcc regime. See Supplementary Materials on how Fe and Ni compositions were calculated.

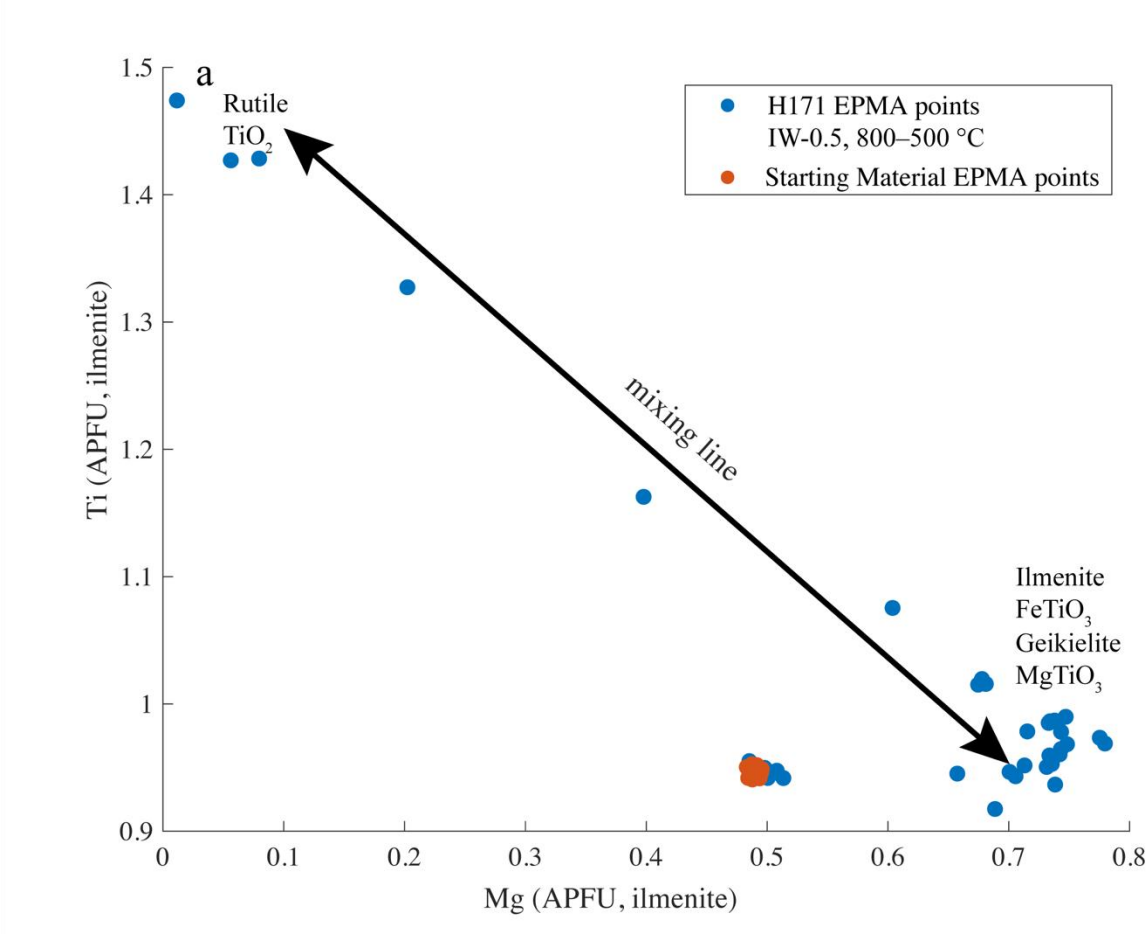

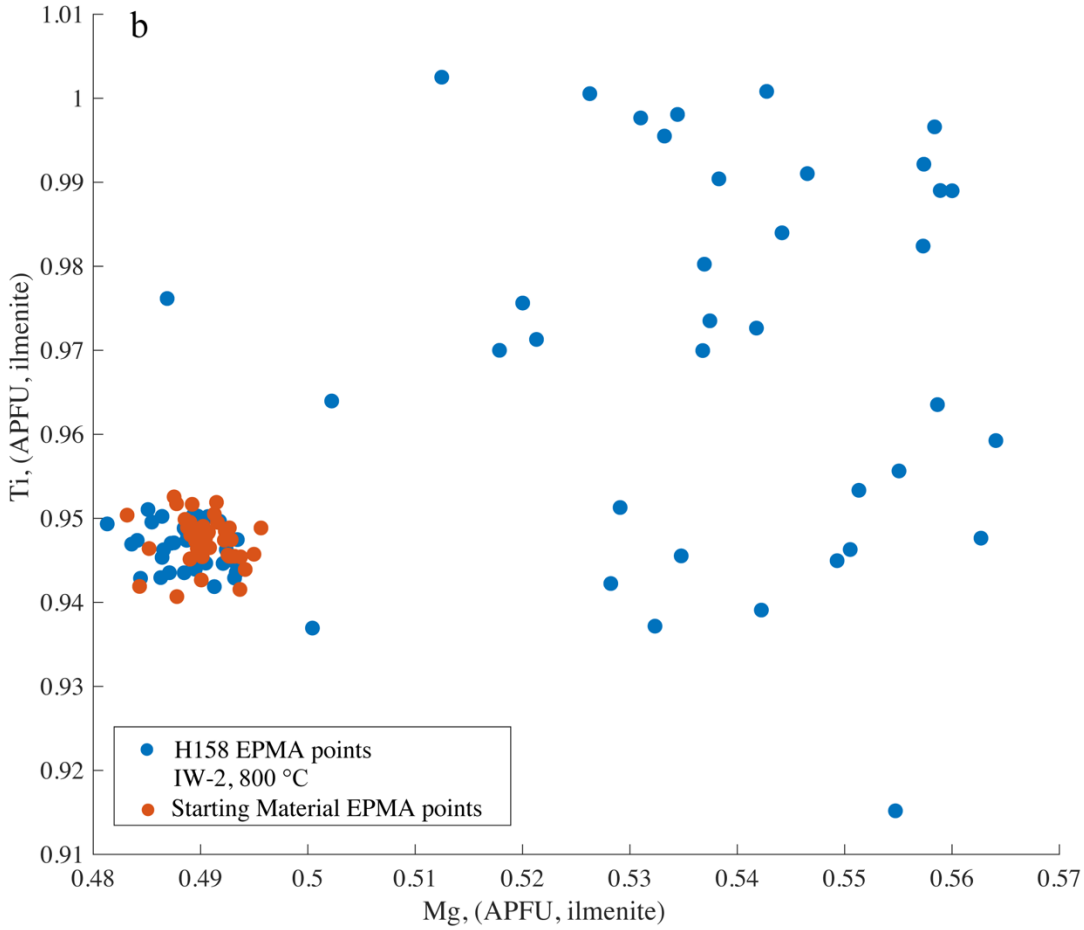

Fig. 2: Scattered plots of the Ti APFU for balanced stoichiometric ilmenite vs. Mg APFU balanced stoichiometric ilmenite and geikielite solid solution of reduction experimental runs H171 (a) and H158 (b) (blue dots) comparing to the starting materials (orange dots). Each dot represented one EPMA data point. Experimental data points (blue) compiled all EPMA traverses from each experiment. Experimental run H171 traverse EPMA data points showed a mixing feature between two end members: rutile and ilmenite+geikielite solid solution. "Mixing line" in Fig. 2a refers to EPMA points that overlapped with/or contained small rutile crystals. Rutile recalculated to ilmenite is $Ti_{1.5}O_3$ with 1.5 APFU Ti. A comparison of the backscattered electron images of runs H171 and H158 can be seen in Fig. 1c and Fig. 1d.

We did traverse analyses by EPMA across the ilmenite reduction reaction zones and found that they have less hematite compared to the starting material. There was an increasing trend of the Ti formula units for balanced stoichiometric ilmenite for all reduced experiments

(Fig. 2). Mg formula units for balanced stoichiometric ilmenite and geikielite solidus solution trending showed both excess and deficit for reduced experiments. Experimental runs H158 and H17 had both increasing Ti and Mg formula patterns (Fig. 2).

Our magnetic hysteresis experiments indicated that the starting material was paramagnetic, as expected for ilmenite at room temperature (M_{rs} = 0). In contrast, all subsolidus reduction products contained ferromagnetic material, as evidenced by their hysteresis loops and parameter values (Figure S1, Table 1). Based on the hysteresis parameter values ($M_{rs}/M_s < 0.5$ and $B_{cr}/B_c > 1.5$), the FeNi grains in the reduced samples were likely in the pseudo-single domain (PSD) to multidomain (MD) size range (Day et al., 1977).

3.2 Reduction isothermal experiments (800 °C) time series at constant fO_2

The reduced experiments run for different experimental durations had M_{rs} values of $5.50*10^{-3}$ Am^2/kg (experimental run J138 for 2 - day), $2.50*10^{-3}$ Am^2/kg (experimental run H154 for 4 - day), $8.23*10^{-4}$ Am^2/kg (experimental run J137 for 8 - day), and $1.65*10^{-3}$ Am^2/kg (experimental run H155 for 16 - day). Following our initial IW-1 experiments, M_{rs} values increased substantially from the zero value of the starting material, indicating that kamacite was likely the created phase rather than taenite (the latter is paramagnetic at room temperature for <30% Ni). Within this batch of experiments, there was no obvious correlation between the M_{rs} values and the experimental durations (Fig. 3). We posit that the observed variations in M_{rs} were most likely dominated by the nonuniform density of random internal fractures inherent in the starting material that can differ between subsamples.

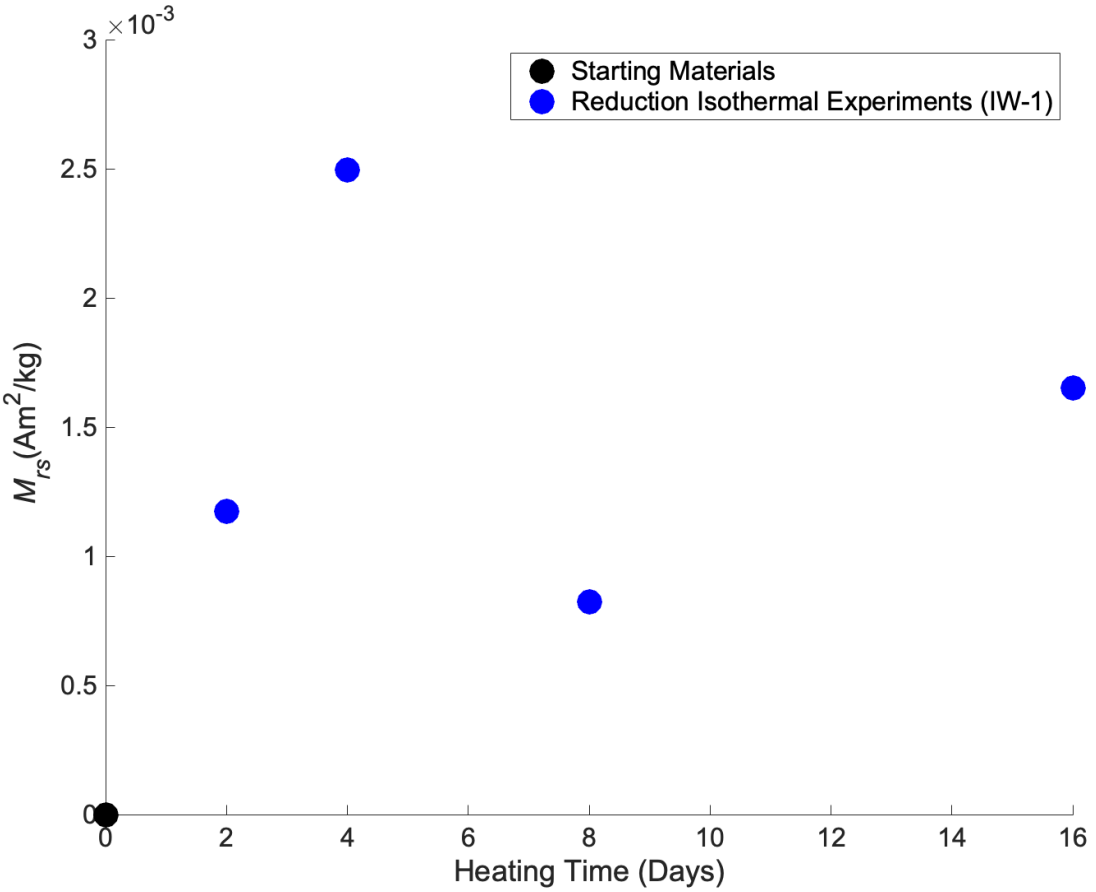

Fig. 3: Time series of isothermal reduction experiments. The comparison of isothermal experiments of different time durations at fO_2 = IW-1 and the starting material. Black dot represented the M_{rs} value for the starting material, and blue dots represented M_{rs} values for the isothermal reduction experiments. All experiments have larger M_{rs} than starting materials, but no trend with time. Suggesting surface area is a dominant factor.

3.3 Reduction experiments with slow cooling

To study the actual cooling process of ilmenite in the Moon's crust, we did two cooling experiments from 800–500 ºC at fO_2 = IW-0.5 (experimental run H171) and 1000–500 ºC at fO_2 = IW-1 (experimental run H174). Despite the uncertainties on the fO_2 conditions (as this run was initially intended to take place at IW-1), H171 had M_{rs} values at least 1 order of magnitude higher than the other isothermal experiments, and H174 had M_{rs} values similar to the other isothermal experiments (Table 1). The origin of the high M_{rs} value of the fO_2 = IW-0.5

experiment was unclear, but it may be possible that the starting material for this experimental run included either smaller than average grain sizes or grains with a high degree of internal fracturing that could have yielded higher surface area to volume ratios for reduction to occur. Therefore, we conducted more experiments using the same temperature and oxygen fugacity conditions but with different ilmenite grain sizes to explore the latter possibility.

3.4 Reduction experiments with varying grain sizes of starting materials

To study the effect of surface area on the extent of ilmenite reduction and metal creation, we conducted two sets of cooling experiments from 800–500 ºC at fO_2 = IW-1 for three different ilmenite grain size ranges (experimental runs H181 and H182). In general, we found that, within each experimental set, the M_{rs} values decreased with increasing ilmenite grain size for both H181 and H182 (Fig. 4).

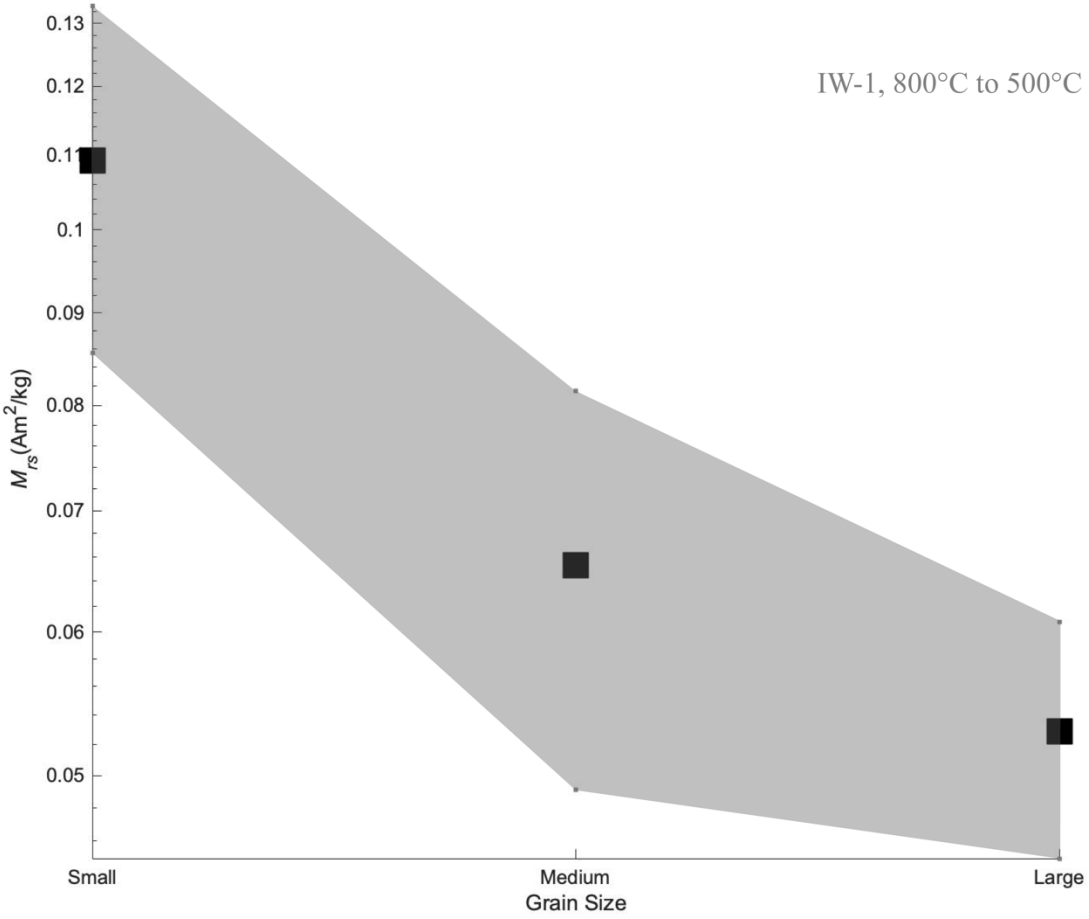

Fig. 4: Comparison of the M_{rs} values of cooling experiments with different grain sizes of starting material. The black squares represent the mean values of M_{rs} for different grain sizes of starting material from two sets of experiments (run H181 and H182 that were at fO_2= IW-1 and had a cooling history from 800–500 ºC. The grey shadow blocked out the actual M_{rs} values of small, medium, and large ilmenite grain sizes of experimental runs H181 and H182.

We also compared the other two cooling experiments (experimental runs H171 and H174) and our most reducing isothermal experiment ran at fO_2 = IW-2 (experimental run H158) with experimental runs H181 and H182 (Table 1) to study the interplay between cooling rate and ilmenite grain size effecting on the magnetization properties of the reduction product. Experimental run H174 had the lowest M_{rs} values; this might be attributable to its high starting

297 temperature at 1000 ºC that could have led to the production of larger, more multidomain (MD)
298 metal grains within the sample. Experimental run H171 had the highest M_{rs} values among all
299 experiments. The M_{rs} values for the small (H181_S and H182_S) and medium (H181_M and
300 H182_M) ilmenite grain size experiments were much higher than the experimental run H158's
301 M_{rs} value, and the large ilmenite grain size (H181_L and H182_L) experiments' M_{rs} values were
302 comparable to H158's M_{rs} value (Table 1). Although the oxygen fugacity of H158 was more
303 reducing compared to experimental runs H171, H181, and H182, slow-cooled experiments still
304 showed higher M_{rs} values with smaller grain sizes and comparable M_{rs} values with similar grain
305 sizes. The reduction products, Fe and rutile, were larger and more visible in the BSE images of
306 the slow-cooled experiments too (Fig. 1c and 1d).
307

308 **4 Discussion**

309 4.1 Ilmenite subsolidus reduction creates FeNi metal
310
311 Reduction of ilmenite to rutile and FeNi metals was observed in some Apollo samples.
312 For reduction products in Apollo crystalline rock samples, the metal phases consisted entirely of
313 kamacite (Ahmed El Goresy et al., 1972). There were two steps in the proposed subsolidus
314 reduction reaction: 1) ulvöspinel reduced to ilmenite and metallic iron, and 2) ilmenite reduced
315 to rutile and metallic iron. Intergrowths of ulvöspinel, ilmenite, and metallic iron had been
316 reported in a limited number of Apollo 11 (e.g. Apollo sample 10058-32 described by Cameron,
317 1970) and 12 samples (e.g., Apollo sample 12050 described by Brown et al., 1971; Apollo
318 sample 12020,10 described by Haggerty and Meyer, 1970) and were observed more broadly in
319 Apollo 14 and 17 basalts (e.g., Apollo samples 14053 and 14072 described by El Goresy et al.,
320 1971; El Goresy and Ramdohr, 1975; Haggerty, 1971). Ilmenite-ulvöspinel aggregates usually

contained native iron, which in most cases was confined to the ilmenite itself or occurred as a compound along the ilmenite-ulvöspinel interface (e.g., Apollo sample 10058-32 described by Cameron, 1970; Apollo sample 15065 described by Taylor et al., 1973). Ilmenite in Apollo 14 samples appeared as a primary phase and also through the process of subsolidus reduction of ulvöspinel (Ahmed El Goresy et al., 1972). The Apollo 14 crystalline rocks 14053 and 14072 displayed the breakdown of chromian ulvöspinel to a greater extent, with all stages of reduction and complete breakdowns (Ahmed El Goresy et al., 1972). Sample 14072 contained ulvöspinel that was broken down into ilmenite and native Fe. Ilmenite grains and fine native Fe grains had been dissolved along the host's {111} plane (Ahmed El Goresy et al., 1972). Similarly, sample 75081 also displayed the thin lamellae of rutile and blebs of metallic iron presenting the ilmenite megacrysts (Taylor, Williams, et al., 1973).

Our experiments were designed to study the effect of temperature, oxygen fugacity, and kinetics of the ilmenite reducing to rutile and metallic iron reduction seen in the Apollo 14 and 17 samples. FeNi metals were produced from our subsolidus reduction experiments, seen in our electron microprobe imaging and quantitative analysis (Fig. 1c, 1d, and Table 3). This was in agreement with the increased M_{rs} values of the reduced experiments compared to the starting materials (Fig. 3d). In conclusion, both our experimental products and Apollo samples provided evidence for the subsolidus reduction of ilmenite to Fe-metal bearing assemblages.

4.2 Slow cooling causes ilmenite subsolidus reduction

Apollo mare basalts such as 15495, 15475, and 15065 had coexisting ulvöspinel, ilmenite, and native Fe, and had Zr partitioning indicating the existence of subsolidus reduction of ulvöspinel to ilmenite and native Fe (McCallister & Taylor, 1973; Taylor et al., 1972; Taylor,

McCallister, et al., 1973). It had been proposed that the slow cooling of mare basalts under 900 ºC was the reason for the subsolidus reduction from ulvöspinels to ilmenite to rutile and metallic iron (McCallister & Taylor, 1973). The study of the Zr ratio of Apollo samples provided evidence of the relationship between the intensity of reduction and cooling rates (Taylor, McCallister, et al., 1973). For example, 15475 and 15065 showed higher reduction intensity of ulvöspinel than 15495, and the former ones had undergone a slower rate of subsolidus cooling (Taylor, McCallister, et al., 1973).

Each of our experiments was run at a constant oxygen offset from the IW buffer curve, but during cooling the absolute fO_2 drops. Slow-cooled experiments produced the highest M_{rs} values among all of the experiments (e.g., compare experimental runs H171 and H182 to H155 and H158) (Table 1 and Section 3.4). Hemingway and Tikoo (2018) also hypothesized that the slow cooling of magmatic features like dikes, sills, and laccoliths could provide the requisite conditions for these subsolidus reduction reaction series to finish. Therefore, in this study, we will testify to the hypothesis of whether these subsolidus reduction reactions in slow cooling conditions can produce enough thermoremanent magnetization for lunar swirls.

4.3 Slow-cooled hypabyssal dikes provide opportunities for ilmenite subsolidus reduction

Previous studies had proposed that the formation of lunar swirls was related to dike cooling and the resulting changes in magnetic properties (e.g., Hemingway and Tikoo, 2018). Our experiments confirmed slow cooling rates are the driving force for ilmenite reduction, and we can place constraints on the necessary dike cooling rates for creating magnetizable materials in the lunar subsurface. Our mechanism, subsolidus reduction of ilmenite, may provide an avenue to produce substantial amounts of fine-grained [pseudo-single domain (PSD) or vortex state (Roberts et al., 2017)] metallic iron in lunar rocks. The crustal magnetic field anomalies

associated with Reiner Gamma and other lunar swirls could potentially be attributable to the reduction of ilmenite in the cooling of dikes and other intrusive magmatic bodies, but certain conditions need to be met: 1) The appropriately reducing environment must be maintained for a sufficient duration to facilitate the reduction reactions (since this is a diffusion-controlled process), and this could require some slow cooling conditions. 2) The surface area of ilmenite grains needs to be high enough to create enough ferromagnetic materials to account for the observed field strength and estimated magnetization intensity of the crustal magnetic anomalies at swirls. In the following section, we will explain how we used Monte Carlo simulations to help us answer whether our proposed mechanism can produce enough magnetization for lunar swirls.

4.4 Monte Carlo modeling of the most important three factors affecting the calculated magnetization values

Thermoremanent magnetization (TRM) is acquired when rocks cool from above the Curie temperature of their ferromagnetic minerals (e.g., ~770ºC for kamacite) in the presence of an ambient magnetic field. We identify three major factors controlling the intensity of TRM that could be acquired as a result of the subsolidus reduction process: 1) the diffusion parameter (*f*) (Section 4.4.1), 2) the domain state of magnetic carriers (Section 4.4.2), and 3) the amount of TiO_2 in mare basalts (Section 4.4.2). We note that subsolidus reduction may occur below the kamacite Curie temperature. In such cases, rocks will instead acquire a thermochemical remanent magnetization (TCRM), which may produce a weaker magnetization intensity than a pure TRM. However, because subsolidus reduction largely occurs at high temperatures (>500ºC) that are close to the Curie temperature, the difference in the resulting TCRM intensity versus a TRM acquired in the same ambient field strength should be negligible (Draeger et al., 2006). Therefore, for simplicity, we hereafter only discuss TRM.

393 4.4.1 Diffusion-controlled ilmenite reduction

394 Our results showed that the ilmenite reduction was driven by a diffusion-controlled
395 reaction progressing from the exterior of the grain to the interior. The reacted zones were
396 concentrated along the surface (grain boundaries and cracks that existed before experiments) (Fig.
397 1b–d). This indicated that the reduction reaction was at least somewhat diffusion controlled. To
398 model this diffusion-controlled process, we used the interdiffusion coefficient of Mg and Fe in
399 ilmenite (Prissel et al., 2020). The experimentally determined Arrhenius fit parameters between
400 Fe and Mg diffusion were 188 kJ mol^{-1} for Q and -6.0 m^2 s^{-1} for $logD_0$ (Prissel et al., 2020).
401 Using the following equation, we calculated the Fe-Mg interdiffusion for our experimental
402 temperature range of 500–800 ºC in ilmenite megacrysts.

403 $$\ln D = \ln D_0 - \frac{Q}{RT} \quad \text{Equation 1}$$

404 where D_0 was the pre-exponential factor (m^2 s^{-1}), Q was the activation energy (J mol^{-1}), R was
405 the universal gas constant (J mol^{-1} K^{-1}) and T was temperature (K). The maximum D value was
406 $7.06*10^{-16}$ m^2 s^{-1} at 800 ºC and the minimum D value was $1.99*10^{-19}$ m^2 s^{-1} at 500 ºC.

407

408 Since ilmenite commonly occurs as a platy crystal in extrusive lunar rocks, we chose to
409 model natural ilmenites by assuming they were infinite plates; approximating that the ilmenite
410 grains were plane sheets. The simple geometry was a good approximation which we verified by
411 also initially modeling crystals as spheres and found the plate geometry was more conservative
412 for reaction progress calculations. The time it would take a platy ilmenite grain with different
413 half-widths to be partially reduced could be approximately calculated by the following equation
414 (McDougall & Harrison, 1999).

415 $$f \simeq \frac{2}{\sqrt{\pi}} * \sqrt{\frac{D*t}{l^2}} \quad \text{Equation 2}$$

where l was the half-width of the ilmenite (m), D (m^2 s^{-1}) was the interdiffusion coefficient between Fe and Mg calculated from Eqn. 1, f is the reduction reaction progress, and t (s) was the duration for the reduction reaction at different levels of progress. This approximate solution of the diffusion equation applies only when $f \leq 0.60$. The reduction time of 60% ilmenite with the maximum D value was ~0.032 years, and the reduction time of 60% ilmenite with the minimum D value was ~113 years.

The diffusion parameter was affected by the sizes of ilmenites and the widths of dikes. The widths of dikes influenced the necessary cooling time of dikes and thus how much time would be available for the ilmenite reduction reaction to proceed (t). We used the modeled cooling history of a dike of a thickness of 10 m from Snelling (1991) and Jaeger (1957). The dike was intruded as a liquid, and we used these published calculations for a cooling interval of 800–500 ºC when the dike was below its solidus. The calculated cooling time for a dike of a thickness of 10 m was $5.37*10^7$ s (~1.73 years). The calculated cooling time for a dike of a thickness of 100 m was ~173 years, which was larger than the 60% reduction time with the minimum diffusion coefficient D, ~113 years. The cooling time for a dike of a thickness of 100 m from 800–500 ºC exceeded 60% of ilmenite reduction time, implying that the cooling time for a dike of a thickness of 100 m was sufficient to reduce ilmenite to rutile and metallic iron.

According to Heiken and Vaniman (1990), the mean ± 1 standard deviation of the half-widths of ilmenite grains in high-Ti mare basalts was approximately 53 μm ± 45 μm. We used these values to represent l in Equation 2. More details on how these values were propagated through calculations of TRM would be discussed in sections 4.4.3 and 4.4.4.

440 4.4.2 The domain state of magnetic carriers and the amount of TiO_2 in mare basalts as
441 two other important factors
442
443 If the subsolidus reduction is a plausible explanation of the subsurface magnetic
444 anomalies associated with the lunar swirls, then the amount of reduction and how much
445 magnetizable material is in slow-cooling dikes, as well as the magnetization recording efficiency
446 of that material are all important factors. In our mechanism, ilmenite reduction is the source of
447 the magnetizable material (metallic Fe or kamacite), and slow-cooling dikes provide the
448 environment for that subsolidus reduction. Thus, the amount of primary TiO_2 in lunar rocks,
449 which dictates how much ilmenite can form, will dictate how much native Fe can be produced.
450 We used the compositions of low-Ti and high-Ti mare basalts to represent two end-member
451 scenarios of Ti contents. The low-Ti basalts tend to have modal mineralogies with $\leq$ 2 vol.%
452 ilmenite (e.g., Papike et al., 1991), whereas there can be up to ~22 vol.% ilmenite in high-Ti
453 basalts (Longhi et al., 1974).

454 Magnetizable materials' domain states are also important factors in determining how
455 much TRM they can record. Rock magnetism studies confirmed that Apollo mare basalt samples
456 contain about 0.1 wt.% of predominantly multidomain (MD) FeNi grains (e.g., Fuller, 1974;
457 Strauss et al., 2021). We produced PSD FeNi grains during our slow-cooling subsolidus
458 reduction experiments (Table 3), which might be a better representation of the metal generated
459 within or proximal to slowly-cooled dikes in the lunar crust than more rapidly cooled, surface-
460 erupted mare basalts. However, due to the uncertainty in the domain state of true lunar
461 subsolidus reduction products, we used both MD and PSD magnetic carriers to model our results
462 (Section 4.4.3 and 4.4.4).
463
464 4.4.3 How to calculate thermoremanent magnetization (M_{tr})

To test whether our mechanism can produce sufficient magnetization intensities to explain lunar swirls, we compared the intensities of TRM calculated from different variables: domain states of magnetic carriers, TiO_2 contents in lunar rocks, and lunar dike cooling rates. We followed the methods of Oliveira et al. (2017) to calculate our experiments' and mare basalts' TRM. Briefly, M_{tr} can be calculated from Equation 3 if we know the following variables: the volumetric concentration of the magnetic carrier *c*, the saturation magnetization of metallic iron $M_{\mathrm{s}}^{\mathrm{Fe}}$, the squareness ratio *s* of the hysteresis loop, the applied magnetic field *B*, and the constant *a*.

$$M_{\mathrm{tr}} = \frac{c\ s\ B\ M_{\mathrm{s}}^{\mathrm{Fe}}}{a} \qquad \text{Equation 3,}$$

where $M_{\mathrm{s}}^{\mathrm{Fe}}$ was 1.715 * 10^6 A m^{-1} (Dunlop & Özdemir, 2015), and *c* was the volumetric concentration of Fe reduced from low-Ti and high-Ti mare basalts. The amounts of metallic Fe can be estimated by the reduction of ilmenite from low-Ti and high-Ti basalts using mass balance and densities. *B* ranged from 10 μT to 100 μT because ~100 μT was the upper limit of lunar paleointensities that had been inferred from paleomagnetic studies of Apollo samples. Constant *a* varied from ~2810 μT for multidomain samples to ~3770 μT for single-domain and pseudo-domain samples (Weiss & Tikoo, 2014; Wieczorek et al., 2022). The squareness *s* was the ratio of the saturation remanent magnetization (M_{rs}) and saturation magnetization (M_{s}) of the experimental samples and mare basalts. To understand the boundaries between domain states, we assumed $M_{\mathrm{rs}}/M_{\mathrm{s}}$ <0.05 was MD; between 0.05 and 0.5 was PSD, and >0.5 was SD (see Fig. 7 of Strauss et al. 2021). $M_{\mathrm{rs}}/M_{\mathrm{s}}$ values from our experiments are listed in Table 1. We selected the experiments that were conducted under fO_2 = IW-1 and IW-2 and there were EPM analyses on the metallic irons (Table 3). The mean $M_{\mathrm{rs}}/M_{\mathrm{s}}$ value from these experiments was 0.295 (PSD). We found that FeNi grains formed during our subsolidus reduction experiments were on

average smaller (pseudo-single domain; M_{rs}/M_s ~0.1) (Table 1) than those naturally occurring within mare basalts (multidomain; M_{rs}/M_s ~0.001-0.01). A typical M_{rs}/M_s value for mare basalts was ~0.0064 (Fuller & Cisowski, 1987). This was of interest because pseudo-single domain grains can more efficiently record thermal remanent magnetization than multidomain grains for a given ambient field intensity (Fig. 5). We noted that in a natural setting, protracted cooling on timescales far exceeding the durations of our laboratory experiments may result in the growth of MD grains rather than PSD grains. While it would be desirable to conduct an experiment analogous to what could occur on the Moon, such long timescales (~100+ years to cool a 100 m dike) is beyond the capability of our analysis.

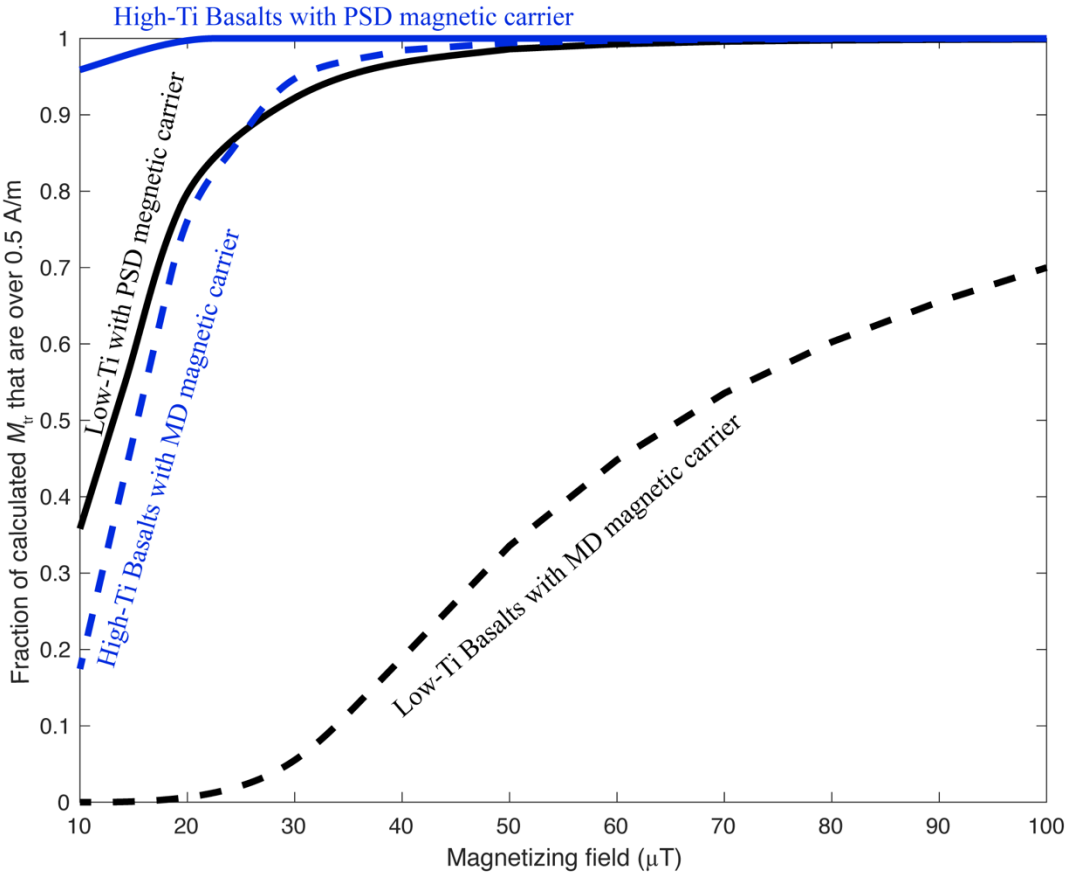

Fig. 5: Different scenarios of percentages of calculated M_{tr} values that are over the minimum requirement for lunar swirls (0.5 A/m) with magnetizing field ranging from 10–100 μT with a dike width = 100 m. Blue line: high-Ti basalts with pseudo-single domain magnetic carriers;

501 blue dashed line: high-Ti basalts with multidomain magnetic carriers; black line: low-Ti basalts
502 with pseudo-single domain magnetic carriers; black dashed line: low-Ti basalts with
503 multidomain magnetic carriers.

4.4.4 Variables were artificially generated to explore a significant proportion of the realistic parameter space

As discussed in the previous section, there are many variables that we do not have precise constraints on because 1) they vary in nature and/or 2) there are uncertainties in the lab analysis. In order to handle uncertainties and variabilities, our strategy was to generate artificial datasets utilizing MATLAB and Monte Carlo simulations to explore the full range of possible parameters.

We used lognormal distributions and Monte Carlo simulations to generate 10^6 random numbers to represent the half-widths of ilmenites (l) in Equation 2 based on the average and one std values of the half-widths of ilmenite grains in high-Ti mare basalts. We used Monte Carlo simulations to find 10^6 uniformly distributed random numbers for each of the following variables: (1) calculated reaction completeness parameter (f) from Equation 2; (2) applied magnetic field B from 10 μT to 100 μT; and (3) two sets of numbers to represent volume percentages of ilmenites one each for low-Ti and high-Ti mare basalts. The ilmenite volume percentages were 0.5–5 vol.% for low-Ti mare basalts and 9–25 vol.% for high-Ti mare basalts. With our current knowledge on the chemical and physical properties of lunar rocks and dike cooling histories, we believed that utilizing Monte Carlo simulation provides an optimal approach to handling variables when calculating the predicted TRM intensities of lunar rocks.

We assumed that <60% of ilmenite was reduced to rutile and metallic Fe (Section 4.4.1) because not all ilmenite had been reduced to rutile and Fe in Apollo samples (Taylor, Williams, et al., 1973). Therefore, we only used f values between 0 and 0.6 calculated from Equation 2 to simulate how much ilmenite in either low-Ti or high-Ti mare basalts was reduced to rutile and Fe metals. Another assumption was that the ilmenite here was only $FeTiO_3$, but there might be a

small amount of MgO existing in the ilmenite (e.g., Alexander et al., 2016; Papike et al., 1991). These assumptions allow us to explore a significant proportion of the realistic parameter space.

4.5 Our proposed reduction mechanism can reproduce lunar swirls' surface magnetic anomalies

As we modeled the effects of the reaction completeness parameter (*f*), the domain state of magnetic carriers, and the amount of TiO_2 in mare basalts on the reduction of ilmenites in the previous section, now we can answer the question of whether this diffusion-controlled subsolidus reaction can produce enough magnetization for lunar swirls.

The intensity of TRM will increase with both higher metallic Fe content as well as with finer average grain sizes (Fig. 5). Lunar swirls were inferred to need magnetization intensities of >0.5 A/m, which could easily be achieved for higher Ti basaltic rocks magnetized in fields of a few microteslas or stronger. According to Hemingway and Garrick-Bethell (2012), the remanent crustal field observed at Reiner Gamma requires an associated source magnetization intensity of 1–100 A/m, depending on source geometry, whereas Airy and other swirls could be explained by somewhat weaker magnetization intensities. Our Monte Carlo simulations reveal several different scenarios that can produce TRM intensities exceeding the minimum 0.5 A/m threshold value (Fig. 5).

For dikes with a low-Ti mare basalt composition and MD FeNi grains, around 20% of calculated TRM reached over 0.5 A/m at around 40 μT ambient fields and if the half-width of ilmenite was within favorable ranges (Fig. 5). However, we noted this was only the case for a small fraction of model runs. In contrast, for low-Ti dikes with PSD FeNi grains, around 80% of

548 our Monte Carlo simulations could reach over 0.5 A/m TRM intensities at around 20 μT ambient
549 field (when varying both the dike cooling time and half-widths of ilmenite) (Fig. 5).

550 There were more possible pathways for the dikes with high-Ti mare basalt compositions
551 to meet the minimum magnetization threshold to explain lunar swirls. For this lithology, ~18%
552 of Monte Carlo runs using rocks with MD grains could produce TRM >0.5 A/m if the paleofield
553 was >10 μT (when varying the half-widths of ilmenite) (Fig. 5). For Monte Carlo runs
554 employing high-Ti mare basalt compositions and PSD FeNi grains, almost all the resulting TRM
555 intensities exceeded 0.5 A/m (even for paleofields as low as 10 μT) when both the dike cooling
556 rate and half-width of ilmenite were varied (Fig. 5).

557 We note that our minimum 0.5 A/m magnetization intensity is much lower than some
558 estimates for the magnetization intensity at the Reiner Gamma swirl (e.g., >10 A/m from
559 Garrick-Bethell and Kelley, 2019). We note that based on the magnetic properties of known
560 lunar rocks, it is not possible to obtain TRM intensities >10 A/m, even for lunar impact melt
561 breccias or melt rocks, from a dynamo field with <100 microtesla intensity (D. J. Hemingway &
562 Tikoo, 2018). The incorporation of iron derived from metal-rich impactors is the most likely
563 scenario to produce >10 A/m magnetization intensities in the lunar crust (D. J. Hemingway &
564 Tikoo, 2018). Therefore, our work narrows down the origin of lunar swirl magnetic source
565 bodies to either impactor ejecta or our hypothesis of subsolidus reduction of dikes/sills with the
566 caveat that this reduction must occur under certain circumstances that may not be exceedingly
567 common (most favorably, a combination of high-Ti initial compositions, PSD domain states, and
568 strong paleofield intensities). Testing between the subsolidus reduction of magmatic intrusive
569 versus impactor metal hypotheses will require making high-resolution lunar crustal magnetic
570 field measurements during surface or near-surface traverses to better constrain the geometries of

the magnetic source bodies. The upcoming Lunar Vertex rover, which will visit Reiner Gamma in 2024, presents the nearest-term opportunity to conduct such an investigation (D. T. Blewett et al., 2022).

5 Conclusions

1. The slow cooling and subsolidus reduction of lunar magmatic intrusive bodies is a plausible mechanism for producing intense lunar crustal magnetism.
2. The ilmenite reduction reaction is a diffusion-controlled reaction; thus, it is dependent on temperature, initial ilmenite grain sizes, and fO_2.
3. Specifically, reduction within hypabyssal dikes with high-Ti or low-Ti mare basalt compositions can produce sufficient FeNi grains to carry the minimum >0.5 A/m magnetization intensity inferred for swirls, especially if ambient fields are >10 μT or if fine-grained Fe-Ni metals in the pseudo-single domain grain size range are formed (Fig. 5). Due to their higher ilmenite content, reduction of high-Ti mare basalts can more easily produce >0.5 A/m magnetizations than reduction of low-Ti mare basalts.
4. Our study highlights that the domain state of the magnetic carriers is an under-appreciated factor in controlling a rock's magnetization intensity. This can be even more important than the metal content of lunar rocks.
5. It is indeed possible for the lunar swirl magnetic anomalies to form from an endogenic origin; however, it may require a specialized combination of initial conditions (i.e., dike width, initial ilmenite content, magnetic domain state, ambient field intensity) that may not commonly occur in tandem.
6. Upcoming missions that will traverse lunar swirls while conducting magnetic field measurements will further elucidate the origin of swirl magnetic source bodies.

596

597 **Open Research:**
598 **Data Availability Statement**
599 We have shared our raw EPMA and Rock Magnetic data at the following link:
600 https://doi.org/10.7936/6RXS-103643. In the WashU Research Data repository, there are .cvs
601 files of RawEPMAData that contain raw EPMA data for the experiments published in the
602 manuscript. RawRockmagData.cvs files contain raw magnetic hysteresis and raw
603 demagnetization data for the experiments published in the manuscript. The raw EPMA and rock
604 magnetization data meet the principles of FAIR data (findable, accessible, interoperable, &
605 reusable).
606
607 **Acknowledgments:**
608 We thank Maxwell Brown and the staff at the Institute for Rock Magnetism (University of
609 Minnesota) for assisting in conducting rock magnetic characterization experiments and Paul
610 Carpenter of Washington University in St. Louis electron microprobe lab for assisting in using
611 the JEOL JXA-8200 electron microprobe.
612
613
614 **Funding:**
615 This work was supported by NASA Grant No. 80NSSC20K0640 to Michael J. Krawczynski and
616 Sonia M. Tikoo. Tikoo was also supported by the LunaSCOPE Solar System Exploration Virtual
617 Institute (SSERVI) No. 80NSSC23M0161.

References:

Alexander, L., Snape, J. F., Joy, K. H., Downes, H., & Crawford, I. A. (2016). An analysis of Apollo lunar soil samples 12070,889, 12030,187, and 12070,891: Basaltic diversity at the Apollo 12 landing site and implications for classification of small-sized lunar samples. *Meteoritics & Planetary Science*, *51*(9), 1654–1677. https://doi.org/10.1111/maps.12689

Blewett, D. T., Halekas, J., Ho, G. C., Greenhagen, B. T., Anderson, B. J., Vines, S. K., et al. (2022). Lunar Vertex: PRISM Exploration of Reiner Gamma, *2678*, 1131. Presented at the 53rd Lunar and Planetary Science Conference. Retrieved from https://ui.adsabs.harvard.edu/abs/2022LPICo2678.1131B

Blewett, David T., Coman, E. I., Hawke, B. R., Gillis-Davis, J. J., Purucker, M. E., & Hughes, C. G. (2011). Lunar swirls: Examining crustal magnetic anomalies and space weathering trends. *Journal of Geophysical Research: Planets*, *116*(E2). https://doi.org/10.1029/2010JE003656

Brown, G. M., Emeleus, C. H., Holland, J. G., Peckett, A., & Phillips, R. (1971). Picrite basalts, ferrobasalts, feldspathic norites, and rhyolites in a strongly fractionated lunar crust. *Lunar and Planetary Science Conference Proceedings*, *2*, 583. Retrieved from https://ui.adsabs.harvard.edu/abs/1971LPSC....2..583B

Cameron, E. N. (1970). Opaque minerals in certain lunar rocks from Apollo 11. *Geochimica et Cosmochimica Acta Supplement*, *1*, 221. Retrieved from https://ui.adsabs.harvard.edu/abs/1970GeCAS...1..221C

Carpenter, P. (2016). JEOL JXA-8200 Electron Microprobe. Retrieved April 18, 2023, from http://xraysrv.wustl.edu/web/probe/probe2.html

641 Day, R., Fuller, M., & Schmidt, V. A. (1977). Hysteresis properties of titanomagnetites: Grain-
642 size and compositional dependence. *Physics of the Earth and Planetary Interiors*, *13*(4),
643 260–267. https://doi.org/10.1016/0031-9201(77)90108-X
644 Denevi, B. W., Robinson, M. S., Boyd, A. K., Blewett, D. T., & Klima, R. L. (2016). The
645 distribution and extent of lunar swirls. *Icarus*, *273*, 53–67.
646 https://doi.org/10.1016/j.icarus.2016.01.017
647 Draeger, U., Prévot, M., Poidras, T., & Riisager, J. (2006). Single-domain chemical,
648 thermochemical and thermal remanences in a basaltic rock. *Geophysical Journal*
649 *International*, *166*(1), 12–32. https://doi.org/10.1111/j.1365-246X.2006.02862.x
650 Dunlop, D. J., & Özdemir, Ö. (2015). 5.08 - Magnetizations in Rocks and Minerals. In G.
651 Schubert (Ed.), *Treatise on Geophysics (Second Edition)* (pp. 255–308). Oxford: Elsevier.
652 https://doi.org/10.1016/B978-0-444-53802-4.00102-0
653 El Goresy, A., & Ramdohr, P. (1975). Subsolidus reduction of lunar opaque oxides: textures,
654 assemblages, geochemistry, and evidence for a late-stage endogenic gaseous mixture.
655 *Lunar and Planetary Science Conference Proceedings*, *1*, 729–745. Retrieved from
656 https://ui.adsabs.harvard.edu/abs/1975LPSC....6..729E
657 El Goresy, Ahmed, Ramdohr, P., & Taylor, L. A. (1971). The geochemistry of the opaque
658 minerals in Apollo 14 crystalline rocks. *Earth and Planetary Science Letters*, *13*(1), 121–
659 129. https://doi.org/10.1016/0012-821X(71)90113-0
660 El Goresy, Ahmed, Taylor, L. A., & Ramdohr, P. (1972). Fra Mauro crystalline rocks:
661 Mineralogy, geochemistry, and subsolidus reduction of the opaque minerals. *Lunar and*
662 *Planetary Science Conference Proceedings*, *3*, 333. Retrieved from
663 https://ui.adsabs.harvard.edu/abs/1972LPSC....3..333E

664 Evans, A. J., Tikoo, S. M., & Andrews-Hanna, J. C. (2018). The Case Against an Early Lunar
665 Dynamo Powered by Core Convection. *Geophysical Research Letters*, *45*(1), 98–107.
666 https://doi.org/10.1002/2017GL075441
667 Fuller, M. (1974). Lunar magnetism. *Reviews of Geophysics*, *12*(1), 23–70.
668 https://doi.org/10.1029/RG012i001p00023
669 Fuller, M., & Cisowski, S. M. (1987). Lunar paleomagnetism. *Geomatik*, *2*, 307–455. Retrieved
670 from https://ui.adsabs.harvard.edu/abs/1987Geoma...2..307F
671 Garrick-Bethell, I., & Kelley, M. R. (2019). Reiner Gamma: A Magnetized Elliptical Disk on the
672 Moon. *Geophysical Research Letters*, *46*(10), 5065–5074.
673 https://doi.org/10.1029/2019GL082427
674 Gose, W. A., & Butler, R. F. (1975). Magnetism of the moon and meteorites. *Reviews of*
675 *Geophysics*, *13*(3), 189–193. https://doi.org/10.1029/RG013i003p00189
676 Haggerty, S. E. (1971). Subsolidus Reduction of Lunar Spinels. *Nature Physical Science*,
677 *234*(49), 113–117. https://doi.org/10.1038/physci234113a0
678 Haggerty, S. E. (2017). Kimberlite discoveries in NW Liberia: Tropical exploration &
679 preliminary results. *Journal of Geochemical Exploration*, *173*, 99–109.
680 https://doi.org/10.1016/j.gexplo.2016.12.004
681 Haggerty, S. E., & Meyer, H. O. A. (1970). Apollo 12: Opaque oxides. *Earth and Planetary*
682 *Science Letters*, *9*(5), 379–387. https://doi.org/10.1016/0012-821X(70)90001-4
683 Heiken, G. H., & Vaniman, D. T. (1990). Characterization of lunar ilmenite resources. *Lunar*
684 *and Planetary Science Conference Proceedings*, *20*, 239–247. Retrieved from
685 https://ui.adsabs.harvard.edu/abs/1990LPSC...20..239H

686 Hemingway, D., & Garrick-Bethell, I. (2012). Magnetic field direction and lunar swirl
687 morphology: Insights from Airy and Reiner Gamma. *Journal of Geophysical Research:*
688 *Planets, 117*(E10). https://doi.org/10.1029/2012JE004165
689 Hemingway, D. J., & Tikoo, S. M. (2018). Lunar Swirl Morphology Constrains the Geometry,
690 Magnetization, and Origins of Lunar Magnetic Anomalies. *Journal of Geophysical*
691 *Research: Planets, 123*(8), 2223–2241. https://doi.org/10.1029/2018JE005604
692 Hood, L. L. (2011). Central magnetic anomalies of Nectarian-aged lunar impact basins: Probable
693 evidence for an early core dynamo. *Icarus*, *211*(2), 1109–1128.
694 https://doi.org/10.1016/j.icarus.2010.08.012
695 Hood, L. L., Torres, C. B., Oliveira, J. S., Wieczorek, M. A., & Stewart, S. T. (2021). A New
696 Large-Scale Map of the Lunar Crustal Magnetic Field and Its Interpretation. *Journal of*
697 *Geophysical Research: Planets*, *126*(2), e2020JE006667.
698 https://doi.org/10.1029/2020JE006667
699 Jaeger, J. C. (1957). The temperature in the neighborhood of a cooling intrusive sheet. *American*
700 *Journal of Science*, *255*(4), 306–318. https://doi.org/10.2475/ajs.255.4.306
701 Longhi, J., Walker, D., Grove, T. L., Stolper, E. M., & Hays, J. F. (1974). The petrology of the
702 Apollo 17 mare basalts. *Lunar and Planetary Science Conference Proceedings*, *1*, 447–
703 469. Retrieved from https://ui.adsabs.harvard.edu/abs/1974LPSC....5..447L
704 Mason, R., & Melson, W. (1970). *The Lunar Rocks*. John Wiley and Sons. Retrieved from
705 https://www.ebay.com/itm/302314846287
706 McCallister, R. H., & Taylor, L. A. (1973). The kinetics of ulvöspinel reduction: Synthetic study
707 and applications to lunar rocks. *Earth and Planetary Science Letters*, *17*(2), 357–364.
708 https://doi.org/10.1016/0012-821X(73)90200-8

McDougall, I., & Harrison, T. M. (1999). *Geochronology and Thermochronology by the 40Ar/39Ar Method*. Oxford University Press.

Oliveira, J. S., Wieczorek, M. A., & Kletetschka, G. (2017). Iron Abundances in Lunar Impact Basin Melt Sheets From Orbital Magnetic Field Data. *Journal of Geophysical Research: Planets*, *122*(12), 2429–2444. https://doi.org/10.1002/2017JE005397

Papike, J., Taylor, L., & Simon, S. (1991). *Lunar Minerals*. *Lunar Sourcebook, A User's Guide to the Moon* (pp. 121–181). Cambridge: Cambridge University Press. Retrieved from https://ui.adsabs.harvard.edu/abs/1991lsug.book..121P

Paterson, G. A., Zhao, X., Jackson, M., & Heslop, D. (2018). Measuring, Processing, and Analyzing Hysteresis Data. *Geochemistry, Geophysics, Geosystems*, *19*(7), 1925–1945. https://doi.org/10.1029/2018GC007620

Prissel, K. B., Krawczynski, M. J., & Orman, J. A. V. (2020). Fe–Mg and Fe–Mn interdiffusion in ilmenite with implications for geospeedometry using oxides. *Contributions to Mineralogy and Petrology*, *175*(7). https://doi.org/10.1007/s00410-020-01695-z

Purucker, M. E., Head III, J. W., & Wilson, L. (2012). Magnetic signature of the lunar South Pole-Aitken basin: Character, origin, and age. *Journal of Geophysical Research: Planets*, *117*(E5). https://doi.org/10.1029/2011JE003922

Roberts, A. P., Almeida, T. P., Church, N. S., Harrison, R. J., Heslop, D., Li, Y., et al. (2017). Resolving the Origin of Pseudo-Single Domain Magnetic Behavior. *Journal of Geophysical Research: Solid Earth*, *122*(12), 9534–9558. https://doi.org/10.1002/2017JB014860

Snelling, A. A. (1991). The Formation and Cooling of Dikes. *Creation Ex Nihilo Technical Journal*, *Vol. 5*(1), 81–90.

Strauss, B. E., Tikoo, S. M., Gross, J., Setera, J. B., & Turrin, B. (2021). Constraining the Decline of the Lunar Dynamo Field at ≈3.1 Ga Through Paleomagnetic Analyses of Apollo 12 Mare Basalts. *Journal of Geophysical Research: Planets*, *126*(3), e2020JE006715. https://doi.org/10.1029/2020JE006715

Tarduno, J. A., Cottrell, R. D., Lawrence, K., Bono, R. K., Huang, W., Johnson, C. L., et al. (2021). Absence of a long-lived lunar paleomagnetosphere. *Science Advances*, *7*(32), eabi7647. https://doi.org/10.1126/sciadv.abi7647

Taylor, L. A., Williams, R. J., & McCallister, R. H. (1972). Stability relations of ilmenite and ulvöspinel in the Fe-Ti-O system and application of these data to lunar mineral assemblages. *Earth and Planetary Science Letters*, *16*(2), 282–288. https://doi.org/10.1016/0012-821X(72)90204-X

Taylor, L. A., Williams, K. L., & Sardi, O. (1973). Selected Apollo 17 soils: Mineralogy and geochemistry of opaque and non-opaque phases. *Earth and Planetary Science Letters*, *21*(1), 6–12. https://doi.org/10.1016/0012-821X(73)90219-7

Taylor, L. A., McCallister, R. H., & Williams, R. J. (1973). The Significance of Zr Partitioning in Apollo 15 Ilmenite and Ulvospinel and The Subsolidus Reduction of Ulvospinel. Retrieved May 1, 2023, from https://articles.adsabs.harvard.edu//full/1973Metic...8...76T/0000076.000.html

Tikoo, S. M., & Evans, A. J. (2022). Dynamos in the Inner Solar System. *Annual Review of Earth and Planetary Sciences*, *50*(1), 99–122. https://doi.org/10.1146/annurev-earth-032320-102418

Weiss, B. P., & Tikoo, S. M. (2014). The lunar dynamo. *Science*, *346*(6214), 1246753. https://doi.org/10.1126/science.1246753

Wieczorek, M. A. (2018). Strength, Depth, and Geometry of Magnetic Sources in the Crust of the Moon From Localized Power Spectrum Analysis. *Journal of Geophysical Research: Planets, 123*(1), 291–316. https://doi.org/10.1002/2017JE005418

Wieczorek, M. A., Weiss, B. P., & Stewart, S. T. (2012). An Impactor Origin for Lunar Magnetic Anomalies. *Science*, *335*(6073), 1212–1215. https://doi.org/10.1126/science.1214773

Wieczorek, M. A., Weiss, B. P., Breuer, D., Cébron, D., Fuller, M., Garrick-Bethell, I., et al. (2022). Lunar magnetism. *Hal-03524536*. Retrieved from https://hal.science/hal-03524536